PAPER

Check for updates

Unique emissive behavior of combustion-derived particles under illumination with femtosecond pulsed near-infrared laser light†

Imran Aslam and Maarten B. J. Roeffaers [ID] *

Exposure to combustion-derived particles (CDPs), such as carbonaceous particulate matter (PM), has adverse effects on human health. Hence, selective detection of these particles in biological environments is required to understand their toxicity. The optical detection of carbonaceous PM is possible in biological samples based on white light (WL) emission under illumination with a femtosecond (fs) pulsed near-infrared (NIR) laser. However, it is unclear if common non-CDPs in ambient PM, such as silica and metal oxides, can interfere with CDP detection when illuminated using a fs-pulsed NIR laser. Here, we show that WL emission, when illuminated with a fs-pulsed NIR laser, is observed only for CDPs amongst other common air pollution particles. We report that the intense WL emission from CDPs spanning over the whole visible spectrum is not observed from non-CDPs. This observation is made for four different CDPs and five different, relevant non-CDPs, in wet and dried samples using biologically relevant imaging conditions. This investigation confirms the uniqueness of WL emission as a selective detection mechanism of CDPs using a multiphoton microscopy platform, commonly available in research laboratories. Furthermore, some relevant signatures for the non-CDPs are provided that could potentially lead to the selective monitoring of pollution related nanoparticles (NPs).

Introduction

Exposure to environmental pollutants is linked to several diseases and an increased mortality rate.[1] Besides various molecular pollutants, ambient particulate matter (PM) is a serious health concern. Recent research has linked various adverse health effects to ambient PM with an obvious concentration and size dependence.[2] For example, ultrafine $PM_{0.1}$ is relatively toxic, because of their increased ability to penetrate the cardiovascular system and reach different organs; PM is typically classified based on their diameter, particles with sizes smaller than 10 μm (PM_{10}), 2.5 μm ($PM_{2.5}$), and ultrafine particles below 0.1 μm ($PM_{0.1}$).[3–5] Further, the pollution source and chemical composition of PM play important roles in determining the toxicity.[6,7]

The primary anthropogenic emission sources of PM in the ambient environment include transportation, fossil fuel burning, and industrial activity.[8–10] Transportation is one of the major contributors to ambient PM concentrations in cities worldwide, either through the exhaust or non-exhaust processes.[9] Vehicle exhaust is considered to contribute mainly

to the emission of ultrafine $PM_{0.1}$ in the urban environment, where non-exhaust emission such as brake and tire wear mostly constitutes coarser $PM_{2.5}$ and PM_{10}.[9,11] Different industrial production processes also make use of the engineered nanomaterials (ENM), which entails the likelihood of release of $PM_{0.1}$ in the environment.[12–14] Furthermore, natural sources of PM may contain salts, and silica making up almost 60% of the dust in the desert regions.[15–17]

Among different constituents of ambient PM, combustion-derived particles (CDPs), such as carbonaceous PM, are considered the most harmful as it is a major source of fine particulate matter.[18] Due to the increasing environmental and occupational exposure to carbonaceous PM, more profound insights into the distribution, uptake, and toxicity of these particles are required.[19–21] Traditionally, absorption photometry and laser-induced incandescence (LII) have been used to determine the concentrations of CDPs in gaseous samples.[22–24] The direct, label-free measurement of carbonaceous PM in biological samples is less trivial. Recently, Bové *et al.* have developed a label-free technique for the detection of carbonaceous PM based on non-incandescence related, white light (WL) emission when illuminated with femtosecond (fs) pulsed near-infrared (NIR) laser light.[25] The detected WL emission is instantaneous, broadband, and has been shown for laser wavelengths in the range from 780 to 900 nm. This technique has been reported to be effective for measuring CDPs in human urine, placenta samples, and plant tissue.[26–28]

Centre for Membrane Separations, Adsorption, Catalysis, and Spectroscopy for Sustainable Solutions, Department of Microbial and Molecular Systems, KU Leuven, Celestijnenlaan 200F, 3001 Leuven, Belgium. E-mail: maarten.roeffaers@kuleuven.be

† Electronic supplementary information (ESI) available. See DOI: 10.1039/d1na00248a

The characterization of ambient PM pollutants in biomedical samples is a challenging task because of the complicated physico-chemical properties of the particles and the absence of specific tools for the characterization of a particular constituent of PM air pollution. However, with the mechanism based on WL emission, the detection of CDPs from ambient PM in biological samples could provide a promising solution. One of the challenges in the selective detection of CDPs in biomedical samples based on the WL emission could be the potential interference from non-CDPs. In this work, we report on the behavior of CDPs and non-CDPs under fs-pulsed NIR laser illumination. Because of the relative presence in ambient PM, the non-CDP nanoparticles (NPs) used in this study included copper oxide (CuO), iron oxides (Fe_3O_4, Fe_2O_3), titanium oxide (TiO_2), and silica (SiO_2).[29–31] This investigation confirms the uniqueness of the WL emission from CDPs illuminated with fs-pulsed NIR laser light compared to non-CDPs. Note that salts form another important group of non-CDPs in air pollution, but due to their high solubility in aqueous environments, they were not included in this study.[32,33]

Materials and methods

PM nanoparticles

All materials were purchased from PlasmaChem GmbH, Germany, unless otherwise stated.

As a reference for CDPs, we used four different types of commercially available carbon black NPs: mesoporous fine carbon nanopowder (fCB; Sigma-Aldrich, Belgium) conductive carbon black (CCB; US Research Nanomaterials, USA), ultrafine Printex 90 (ufP90; Orion Engineered Carbons, Germany) and ultrafine carbon particles (ufPL; PlasmaChem GmbH, Germany). These particles are reported to be used as a model component for black carbon or soot.[34,35] The aerodynamic diameter of these particles, according to the manufacturer's data, is <500 nm, 150 nm, 14 nm, and 13 nm for fCB, CCB, ufP90, and ufPL, respectively. However, they tend to aggregate in aqueous suspensions.[36] As a model component for various common oxide species in the ambient PM, we employed commercially available CuO (40 nm), Fe_3O_4 (8 nm, US Research Nanomaterials, USA), Fe_2O_3 (6 ± 2 nm), TiO_2 (6 ± 2 nm), and SiO_2 (10 nm).

Sample preparation

The NP stock suspensions were prepared in ultrapure water (MilliQ; Merck Millipore, Belgium) and buffer medium (10% fetal bovine serum in Isocov's modified medium (IMDM), Fisher Scientific, Belgium) with concentrations of 2 mg ml^{-1}. The stock solutions were ultrasonicated for 30 minutes and stored in dark at 4 °C until further use. Before using, stock suspensions were ultrasonicated for 30 min and further diluted to prepare the desired concentration of 20 µg ml^{-1}. Afterwards, the diluted suspension was vortexed for 1 min, ultrasonicated for 20 minutes at 40 kHz to break aggregates, and vortexed again for 1 min to properly suspend the particles. Subsequently, the optical measurements on 250 µl volume of suspension were

performed immediately (<3 min) in a chamber of an Ibidi µ-Slide 8 well (Ibidi GmbH, Germany) to avoid aggregation and settling of the particles. The above procedure was repeated for the next measurement. For measurements on dry NPs, the suspensions were drop-casted and dried on a coverglass. Suspensions with a concentration of 2 mg ml^{-1} were used to measure the particles' emission spectra.

Dual-channel detection

The dual-channel multiphoton microscopy measurements were performed on a commercial inverted microscope (Leica TCS SP8, Leica Microsystems GmbH, Germany). The light from a tunable laser (MaiTai DeepSee, 810 nm, 80 MHz, 100 fs, SpectraPhysics – USA) was focused on the sample using a water-immersion objective (HC PL APO 63x, Leica Microsystems GmbH, Germany). The light emitted by the particles is collected by the same objective and separated from the laser light by an Acousto-Optical Beam Splitter (AOBS, Leica Microsystems CMS GmbH, Germany). Afterwards, the light reflected by a dichroic beam splitter (Di02-R442, Semrock Inc., USA) was filtered with a bandpass filter (FF01-405/10, Semrock Inc., USA), and transmitted light filtered with a bandpass filter (FF01-550/200 nm, Semrock Inc., USA) before detection with non-descanned detectors (Leica HyD SMD, Leica Microsystems GmbH, Germany). The image acquisition was carried out using a commercial software Leica Application Suite X software (Leica Microsystems GmbH, Germany). The images were acquired using a pixel format of 512 × 512 pixels, with 0.316 × 0.316 µm^2 pixel size and 3.16 µs pixel dwell time. The total image frame size was 184.52 × 184.52 µm^2. Each measurement consisted of 10 consecutive frames recorded at the same location in a single well. For each well of the µ-Slide 8 well, 2 random locations were measured. For each sample, measurements in 4 wells were repeated, leading to 8 measurements and 80 image frames. All images were collected at room temperature. The measurements on dried NPs were performed at 5 different locations at room temperature.

The quantification of the particles in suspensions, based on dual-channel detection, was carried out using Fiji ImageJ (https://imagej.net/Fiji). We performed a pixel-by-pixel comparison of the images from channel 1 and channel 2 using Pearson's correlation coefficient. Afterwards, the threshold of the correlated pixels was set to 85% of the maximum pixel intensity in the correlated image. After that, we counted the number of particles in each image based on the correlated signal in both channels at these positions (connected pixels) in the sample. The average number of particles counted in the image stack (10 frames) was converted to a number of particles counted per ml; one image frame probes a sample volume related to the image size 184.52 × 184.52 µm^2 and imaging depth of ~1 µm. For each sample, particles per ml were expressed as the mean of 8 measurements, each consisting of 10 frames, with corresponding standard deviation. The data were further processed and analyzed using Origin (ver. 2020, OriginLab Corporation, USA).

Emission spectra measurements

The emission spectra were measured on a commercial microscope (DMi8, Leica Microsystems GmbH, Germany) equipped with tunable NDD detectors in a commercial system (Leica SP8 Dive, Leica Microsystems GmbH, Germany). The 810 nm light from a tunable laser (MaiTai Insight X3, 80 MHz, 120 fs, SpectraPhysics, USA) was focused using a water immersion objective (HC PL IRAPO 40x, Leica Microsystems GmbH, Germany) on the sample. The light emitted by the particles is collected by the same objective and separated from the laser light using an Acousto-Optical Beam Splitter (AOBS, Leica Microsystems CMS GmbH, Germany). Afterwards, the emitted light is sent to the 4Tune non-descanned detection unit in the microscope; the 4Tune detection unit allows spectral detection using non-
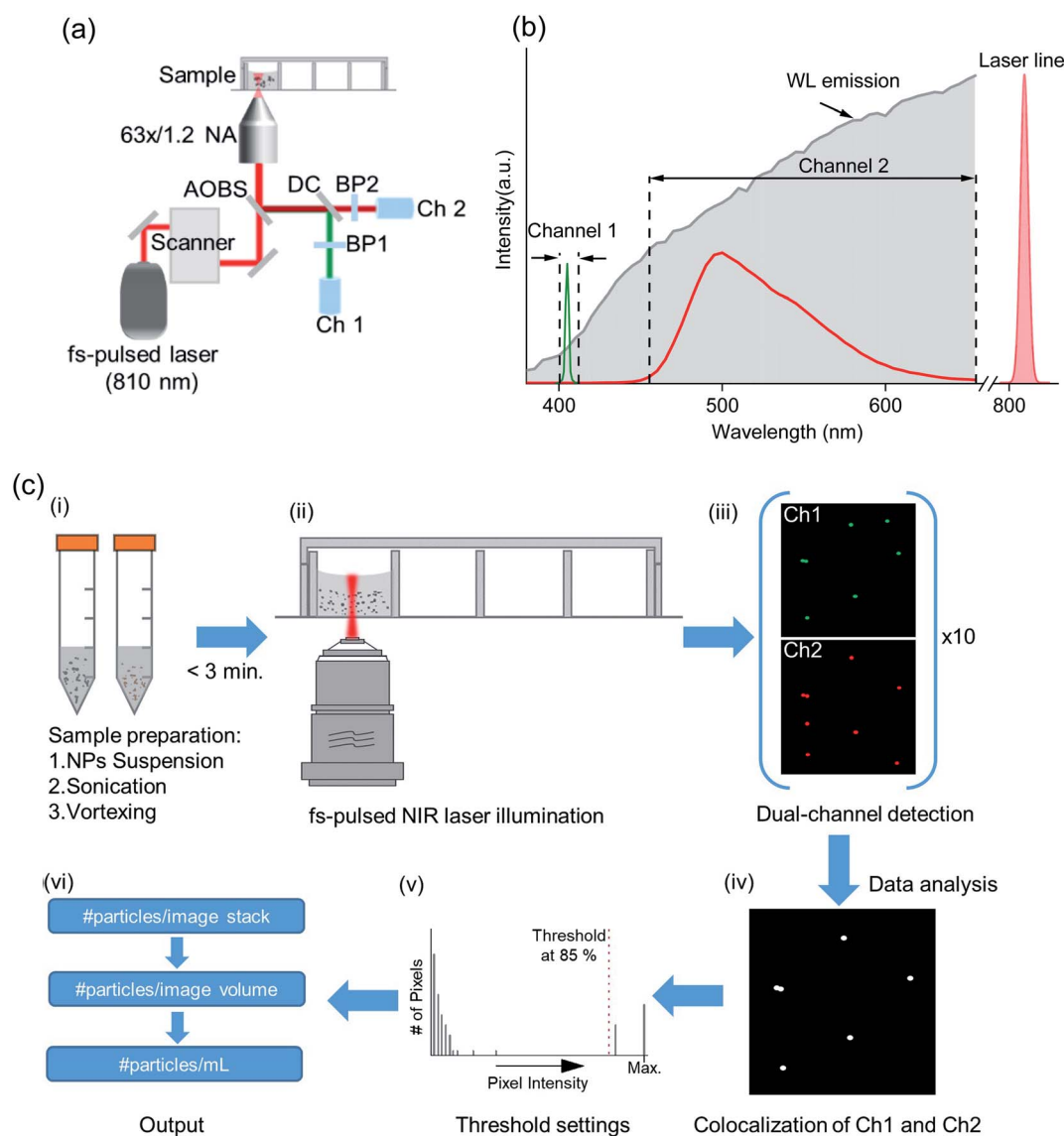

Fig. 1 (a) Schematic of the multiphoton microscope with dual-channel detection. Acousto-optical beam splitter (AOBS) separates the 810 nm nIR light from the laser. Dichroic (DC) beamsplitter splits the emitted light into two different paths. Channel 1 has a bandpass filter 1 (BP1) with central wavelength of 405 nm and a detection bandwidth of 10 nm. Channel 2 has a bandpass filter 2 (BP 2) with central wavelength of 550 nm and a detection bandwidth of 200 nm (b) schematic showing the dual-channel detection of WL emitted by the particles. Excitation with a laser wavelength at 810 nm, the WL emitted by CDPs covers the whole visible spectrum and can be detected in channel 1 (SHG channel, 400–410 nm) and channel 2 (TPAF channel, 450–650 nm), simultaneously. (c) Flowchart of the experimental protocol for dual-channel multiphoton measurements on suspensions of various common CDPs and non-CDPs employed as a model component for PM air pollution. (i) Sample preparation steps include preparation of NP suspensions, 30 min sonication, and 1 min vortexing. (ii) Each sample was aliquoted at 250 μl per chamber in an Ibidi μ-Slide 8 well. The samples were illuminated with a femtosecond laser (810 nm, 80 MHz, 9.5 mW) and measured at 100 μm above the top glass surface of Ibidi μ-Slide 8 well. (iii) Dual-channel detection at each measurement position for channel 1 (Ch1) and channel 2 (Ch2). (iv) One-to-one pixel comparison of channel 1 and channel 2 using colocalization analysis in Fiji ImageJ, where connected pixels represent a single particle. (v) The threshold value was set at 85% of the maximum pixel intensity. This threshold value resulted in reproducible results without false positives and negatives. (vi) Further analysis of the images was carried-out to count the number of particles detected per ml.

descanned detectors (Leica HyD SMD, Leica Microsystems GmbH, Germany). The light emitted by the particles was detected over the whole visible region from 380 nm to 640 nm with a detection step size of 5 nm. The resulting lambda image was obtained with 512 × 512 pixels, 0.569 × 0.569 μm^2 pixel size, and 3.16 μs pixel dwell time. All data were collected using the Leica Application Suite X software (Leica Microsystems GmbH, Germany). The multiphoton emission spectra measurements were performed on NP suspensions inside an Ibidi μ-Slide 8 well as well as on dried NPs. For measurements on dry NPs, the NPs were dried on a cover glass. All measurements were performed at room temperature. The data were processed and analyzed using MATLAB (R2020a, MathWorks, USA) and Origin (ver. 2020, OriginLab Corporation, USA). The data analysis of emission spectra measurements is discussed in the ESI.†

Results and discussion

The dual-channel multiphoton microscopy measurements on CDPs and non-CDPs as reference for particulate air-pollutants were performed on NP suspensions in buffered medium and ultrapure water at biologically relevant concentrations of 20 μg ml^{-1}.[37,38] The light emitted by the particles was detected simultaneously in two separate channels, which are available with most multiphoton microscopes in biomedical research laboratories, as shown in the schematic in Fig. 1a and b. Channel 1 with narrow-band detection (400–410 nm) is commonly used for the detection of second harmonic generation (SHG), while channel 2 with broadband detection (450–650 nm) is used for the detection of two-photon autofluorescence (TPAF) for many applications.[39,40] Detection of light emitted by the particles in two different channels simultaneously is
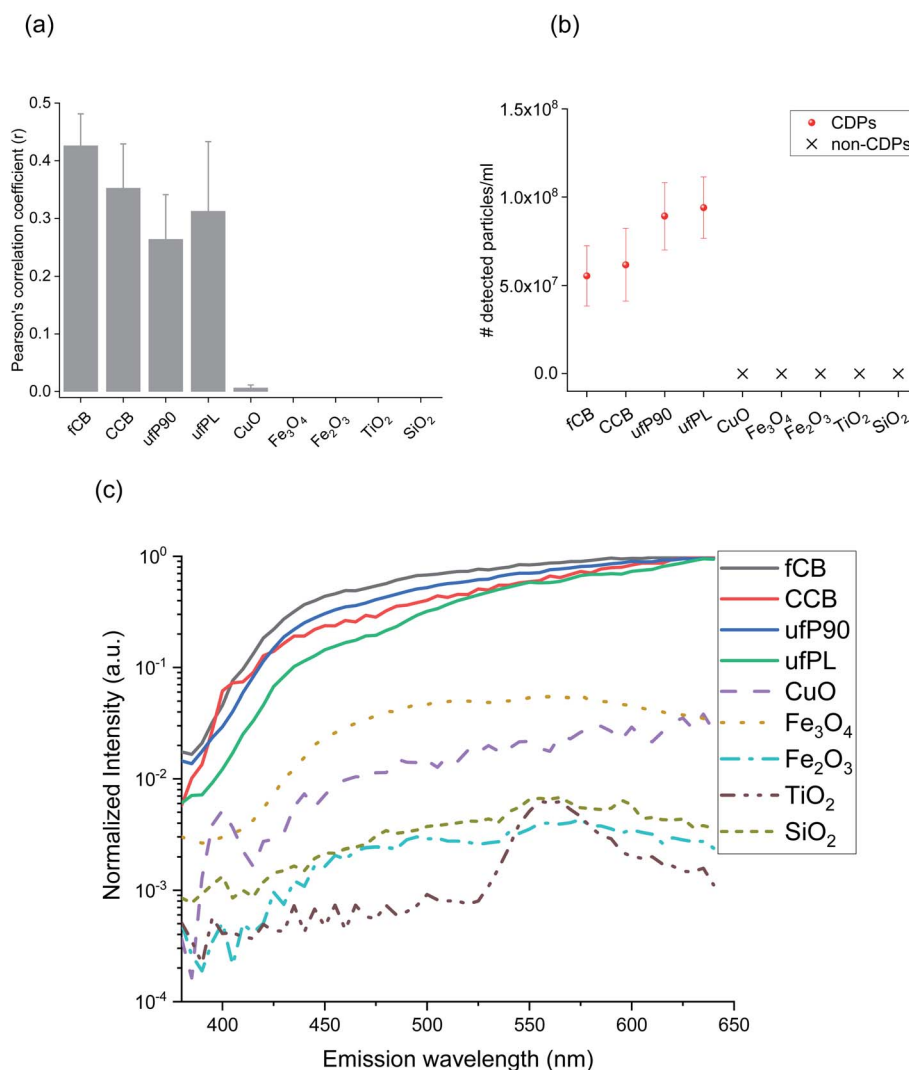

Fig. 2 Dual-channel and emission spectra measurements on CDPs and non-CDPs in suspensions with fs-pulsed NIR laser (810 nm, 80 MHz). (a) The Pearson's correlation coefficient between channel 1 and channel 2 for CDPs and non-CDPs calculated using coloc2 plugin in Fiji ImageJ. (b) The number of particles counted per ml in a biologically relevant concentration (20 μg ml^{-1}). The data are average ± SD ($n = 8$). (c) The emission spectra of the NP suspensions for both CDPs and non-CDPs employed in this study under fs-pulsed NIR laser illumination with an average laser power of 8 mW in focus. The background measured using ultrapure water was removed from the emission spectra of NPs.

necessary to eliminate the unwanted interference. The dual-channel multiphoton microscopy measurements on CDPs and non-CDPs in suspensions were performed according to the customized protocol (Fig. 1c). Fig. 2a shows the correlation between channel 1 and channel 2 for dual-channel detection of CDPs and non-CDPs suspensions. We could observe a significant correlation between channel 1 and channel 2 in the case of all tested CDP samples as compared to the non-CDP samples.
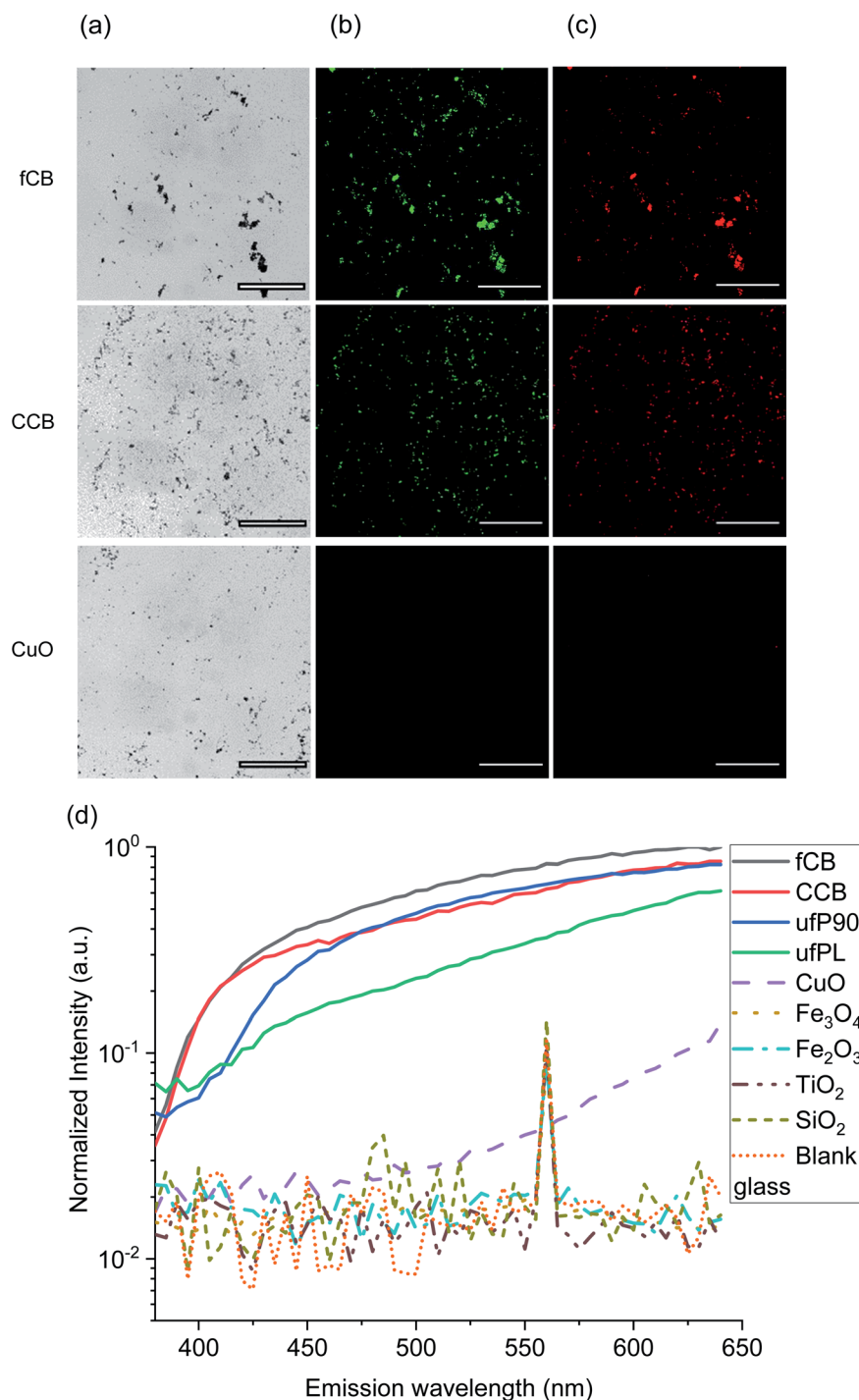

Fig. 3 Dual-channel and emission spectra measurements of dried CDPs and non-CDPs using fs-pulsed NIR laser illumination (810 nm, 80 MHz) (a) Transmitted light microscopy images of dried fCB, CCB, and CuO particles on a cover glass showing the presence of particles. (b) WL emitted by fCB and CCB is visible in channel 1. (c) WL emitted by fCB and CCB is also visible in channel 2. Very weak emission from CuO can be seen in channel 2. Brightness and contrast of the images is enhanced for better visibility. For dual-channel detection, an average laser power of 1 mW is used. (d) Emission spectra measurements on dried CDPs and non-CDPs measured using fs-pulsed NIR illumination. The average laser power used for the measurements on CDPs and non-CDPs is 0.8 mW, respectively. Scale bar: 50 µm.

Nanoscale Advances

Paper

This is due to the strong WL emission from CDPs, which leads to signals detected in both channels simultaneously (see also scheme in Fig. 1b), a feature not present for non-CDPs. Based on the correlated images, we counted the number of particles detected in the buffered medium and ultrapure water as shown in Fig. 2b and S1,† respectively. Fig. 2b shows the CDPs detected in buffered medium with an overall average (SD) of 5.54×10^7 (1.71×10^7) for fCB, 6.17×10^7 (2.05×10^7) for CCB, 8.92×10^7 (1.90×10^7) for ufP90, and 9.40×10^7 (1.75×10^7) for ufPL. The number of particles detected for CDPs in suspensions based on dual-channel detection is lower than expected based on the manufacturer's data (Fig. S3†). This difference can be attributed to the aggregation of NPs; Table S1, Fig. S4 and S5† show the tendency of all tested NPs to aggregate.

In addition to the dual-channel detection, the visible emission spectra for the suspensions of all samples were recorded; Fig. S7a† and 2c show the recorded emission spectra and the background-corrected spectra, respectively. Around 405 nm, the typical SHG channel, the emission spectra of CDPs and non-CDPs show a significant difference in intensity with negligible emission from most non-CDPs (SiO_2, TiO_2, Fe_2O_3, and Fe_3O_4). Only CuO shows a weak intensity peak which can be assigned to weak second harmonic generation.[41,42] Nevertheless, the peak intensity from CuO is almost 5-fold lower than the emission intensity from CDPs under similar imaging conditions. If we look at the emission spectra in the spectral region between 450 to 640 nm, the difference between the emission intensity of CDPs and non-CDPs is equally large. This is due to the strong WL emission from CDPs over the whole visible spectrum. Non-CDPs show only minimal intensities in this spectral region at levels comparable to the blank solution. Fe_3O_4 and CuO display an additional weak photoluminescence which is still orders of magnitude weaker than the WL of CDPs in this spectral region.[43–46]

Next, the optical measurements on dried CDPs and non-CDPs as an extreme condition to fixed biological samples were also performed at moderate laser power densities of 0.4–1 MW cm^{-2} similar to those used in biomedical research. Fig. 3a–c and S9,† show the transmitted light microscopy images and dual-channel images of dried CDPs and non-CDPs deposited on a coverglass. Channel 1 shows strong emission from dried CDPs, while no emission is observed from dried non-CDPs. Channel 2 also shows strong emission from dried CDPs, and a very weak emission signal is observed for CuO which could be attributed to photoluminescence as already observed in suspensions. A negligible emission can also be observed from dried Fe_3O_4 in channel 2, while other dried non-CDPs (SiO_2, TiO_2, Fe_2O_3) do not show any emission either in channel 1 or channel 2 at similar conditions (Fig. S9†).

Fig. 3d shows the recorded emission spectra of dried CDPs and non-CDPs. In general, the emission of dried CDPs at 405 nm is almost 5-fold higher as compared to non-CDPs, and while the emission from dried CDPs keeps increasing over the whole visible spectrum it remains constant at the background level for non-CDPs. Although dried CuO shows a similar emission as other non-CDPs around 405 nm, the weak photoluminescence intensity from dried CuO starts increasing slowly

around 500 nm but still almost an order of magnitude lower than the emission intensity from dried CDPs. The increase in the emission intensity of CuO continues till 640 nm where it is at least 4-fold lower than the emission intensity from dried CDPs (ufPL). Note that the spectra show a small and narrow emission peak around 550 nm which is due to an artifact from the instrument.

Further, we have performed time-correlated single photon counting experiments to look at the temporal response of emission signals from CDPs and non-CDPs (Fig. S10 and S11†). Similar to the previous study,[25] the temporal response of WL emission from CDPs is instantaneous. However, the weak signals from non-CDPs have a longer temporal response in the nanosecond domain which supports the idea of photoluminescence or fluorescence. The temporal response of the emission signal from all four CDPs employed in this study is around 60 ps, whereas the temporal response of the weak emission signals from CuO, Fe_3O_4, Fe_2O_3, TiO_2, and SiO_2 is 1.75 ns, 1.3 ns, 2.3 ns, 1.56 ns and 3.4 ns respectively. This difference in lifetime can be used by researchers to discriminate between CDPs and non-CDPs, as well as amongst different non-CDPs.

In our previous study, we have shown the WL emission from the CDPs on the anti-Stokes side of the laser.[25] In this work we also investigated the Stokes side of the laser for CDPs and we could observe that unique light emission from CDPs arises as a result of broad Stokes and anti-Stokes emission (Fig. S12†). We believe that the broad anti-Stokes and stokes emission from CDPs might arise due to the temporary generation of hot electron gas on arrival of a fs pulse. Similar emission behavior has already been reported for noble-metal nanostructures and films with non-linear power dependence.[47,48] We could also confirm that the WL emission from CDPs exhibits a non-linear power dependence (Fig. S13†).

Conclusions

In conclusion, we have demonstrated the difference in light emission under illumination with fs-pulsed NIR lasers of CDPs and non-CDPs as the major components of PM air pollution. We have observed that 4 different types of CDPs used in this study all display a similar instantaneous WL emission when illuminated under fs-pulsed NIR lasers. In comparison, the 5 different non-CDPs, used as a model component for PM air-pollutants, do not show this emission behavior under similar conditions. The measurements were done on wet and dried samples as different extreme conditions relevant for live and fixed biomedical samples. The emission from both CDPs and non-CDPs was investigated using emission spectra measurements and dual-channel detection in a multiphoton microscopy system. The emission spectra of the CDPs and non-CDPs were studied under fs-pulsed NIR laser illumination in the visible spectrum from 380 to 640 nm. The CDPs show strong light emission, increasing from the typical SHG channel into the two-photon fluorescence signal towards the laser excitation wavelength; a spectral response not displayed by non-CDPs. Based on this observation, a simple dual-channel detection suffices to discriminate CDPs from non-CDPs. Further, the temporal

filtering with the WL emission of CDPs being instantaneous *versus* the weak photoluminescence with ns-timescale lifetime of non-CDPs can be used to further distinguish both groups of materials. The unique emissive behavior of CDPs and relevant signatures of non-CDPs can be used for detecting relevant pollution related NPs using selective optical microscopy techniques. We also believe that the uniqueness of WL emission from CDPs could open new avenues for the development of diagnostic tools for exposure estimation of CDPs at the level of individual persons.

Conflicts of interest

There are no conflicts to declare.

Acknowledgements

References

1 B. Brunekreef and S. T. Holgate, Air pollution and health, *Lancet*, 2002, **360**(9341), 1233–1242, DOI: 10.1016/S0140-6736(02)11274-8.

2 P. E. Schwarze, *et al.*, Particulate matter properties and health effects: consistency of epidemiological and toxicological studies, *Hum. Exp. Toxicol.*, 2006, **25**(10), 559–579, DOI: 10.1177/096032706072520.

3 C. Terzano, F. Di Stefano, V. Conti, E. Graziani and A. Petroianni, Air pollution ultrafine particles: toxicity beyond the lung, *Eur. Rev. Med. Pharmacol. Sci.*, 2010, **14**(10).

4 K. Donaldson, V. Stone, A. Clouter, L. Renwick and W. MacNee, Ultrafine particles, *Occup. Environ. Med.*, 2001, **58**(3), 211–216, DOI: 10.1136/oem.58.3.211.

5 L. L. Nani Guarieiro and A. L. Nani Guarieiro, Vehicle Emissions: What Will Change with Use of Biofuel?, *Biofuels: Econ., Environ. Sustainability*, 2013, DOI: 10.5772/52513.

6 R. D. Brook, Cardiovascular effects of air pollution, *Clin. Sci.*, 2008, **115**(6), 175–187, DOI: 10.1042/CS20070444.

7 Y. Lyu, *et al.*, Seasonal and spatial variations in the chemical components and the cellular effects of particulate matter collected in Northern China, *Sci. Total Environ.*, 2018, **627**, 1627–1637, DOI: 10.1016/j.scitotenv.2018.01.224.

8 R. M. Dickhut, *et al.*, Automotive sources of carcinogenic polycyclic aromatic hydrocarbons associated with particulate matter in the Chesapeake Bay region, *Environ. Sci. Technol.*, 2000, **34**(21), 4635–4640, DOI: 10.1021/es000971e.

9 N. J. Hime, G. B. Marks and C. T. Cowie, A comparison of the health effects of ambient particulate matter air pollution from five emission sources, *Int. J. Environ. Res. Public Health*, 2018, **15**, DOI: 10.3390/ijerph15061206.

10 F. Popescu and I. Ionel, Anthropogenic Air Pollution Sources, *Air Qual.*, 2010, DOI: 10.5772/9751.

11 I. A. Reşitoğlu, K. Altinişik and A. Keskin, The pollutant emissions from diesel-engine vehicles and exhaust aftertreatment systems, *Clean Technol. Environ. Policy*, 2015, **17**, 15–27, DOI: 10.1007/s10098-014-0793-9.

12 S. M. Louie, R. Ma and G. V. Lowry, Transformations of Nanomaterials in the Environment, *Front. Nanosci.*, 2014, **7**, 55–87, DOI: 10.1016/B978-0-08-099408-6.00002-5.

13 A. A. Keller, S. McFerran, A. Lazareva and S. Suh, Global life cycle releases of engineered nanomaterials, *J. Nanoparticle Res.*, 2013, **15**, DOI: 10.1007/s11051-013-1692-4.

14 S. J. Klaine, *et al.*, Nanomaterials in the environment: Behavior, fate, bioavailability, and effects, *Environ. Toxicol. Chem.*, 2008, **27**(9), 1825–1851, DOI: 10.1897/08-090.1.

15 E. Athanasopoulou, M. Tombrou, S. N. Pandis and A. G. Russell, The role of sea-salt emissions and heterogeneous chemistry in the air quality of polluted coastal areas, *Atmos. Chem. Phys.*, 2008, **8**(19), 5755–5769, DOI: 10.5194/acp-8-5755-2008.

16 D. Sing and C. F. Sing, Impact of direct soil exposures from airborne dust and geophagy on human health, *Int. J. Environ. Res. Public Health*, 2010, **7**, 1205–1223, DOI: 10.3390/ijerph7031205.

17 E. E. A. Technical, *Particulate Matter from Natural Sources and Related Reporting under the EU Air Quality Directive in 2008 and 2009*, 2012.

18 S. Schmidt, R. Altenburger and D. Kühnel, From the air to the water phase: implication for toxicity testing of combustion-derived particles, *Biomass Convers. Biorefin.*, 2019, **9**, 213–225, DOI: 10.1007/s13399-017-0295-1.

19 R. Puntoni, *et al.*, Occupational exposure to carbon black and risk of cancer, *Cancer Causes Control*, 2004, **15**, 511–516, DOI: 10.1023/B:CACO.0000036446.29787.94.

20 H. Olstrup, C. Johansson and B. Forsberg, The use of carbonaceous particle exposure metrics in health impact calculations, *Int. J. Environ. Res. Public Health*, 2016, **13**, 249, DOI: 10.3390/ijerph13030249.

21 D. Sahu, G. M. Kannan and R. Vijayaraghavan, Carbon black particle exhibits size dependent toxicity in human monocytes, *Int. J. Inflam.*, 2014, DOI: 10.1155/2014/827019.

22 J. C. Chow, *et al.*, Aerosol light absorption, black carbon, and elemental carbon at the Fresno Supersite, *California. Atmos. Res.*, 2009, **93**(4), 874–887, DOI: 10.1016/j.atmosres.2009.04.010.

23 C. Schulz, *et al.*, Laser-induced incandescence: Recent trends and current questions, *Appl. Phys. B: Lasers Opt.*, 2006, **83**, 333–354, DOI: 10.1007/s00340-006-2260-8.

24 *Report of the Working Party on Methods of Measuring Air Pollution and Survey Techniques*, Organisation for Economic Co-Operation and Development, 1964.

25 H. Bové, *et al.*, Biocompatible Label-Free Detection of Carbon Black Particles by Femtosecond Pulsed Laser Microscopy, *Nano Lett.*, 2016, **16**(5), 3173–3178, DOI: 10.1021/acs.nanolett.6b00502.

26 N. D. Saenen, *et al.*, Children's urinary environmental carbon load: a novel marker reflecting residential ambient air pollution exposure?, *Am. J. Respir. Crit. Care Med.*, 2017, **196**(7), 873–881, DOI: 10.1164/rccm.201704-0797OC.

27 H. Bové, *et al.*, Ambient black carbon particles reach the fetal side of human placenta, *Nat. Commun.*, 2019, **10**, DOI: 10.1038/s41467-019-11654-3.

28 K. Witters, *et al.*, Monitoring indoor exposure to combustion-derived particles using plants, *Environ. Pollut.*, 2020, **266**(1), DOI: 10.1016/j.envpol.2020.115261.

29 B. Fahmy and S. A. Cormier, Copper oxide nanoparticles induce oxidative stress and cytotoxicity in airway epithelial cells, *Toxicol. Vitr.*, 2009, **23**(7), 1365–1371, DOI: 10.1016/j.tiv.2009.08.005.

30 J. Baltrusaitis, P. M. Jayaweera and V. H. Grassian, Sulfur dioxide adsorption on TiO_2 nanoparticles: influence of particle size, coadsorbates, sample pretreatment, and light on surface speciation and surface coverage, *J. Phys. Chem. C*, 2011, **115**(2), 492–500, DOI: 10.1021/jp108759b.

31 G. P. Huffman, *et al.*, Characterization of fine particulate matter produced by combustion of residual fuel oil, *J. Air Waste Manag. Assoc.*, 2000, **50**(7), 1106–1114, DOI: 10.1080/10473289.2000.10464157.

32 P. Schlag, *et al.*, Ambient and laboratory observations of organic ammonium salts in PM1, *Faraday Discuss.*, 2017, **200**, 331–351, DOI: 10.1039/c7fd00027h.

33 J. Klimeš, D. R. Bowler and A. Michaelides, Understanding the role of ions and water molecules in the NaCl dissolution process, *J. Chem. Phys.*, 2013, **139**(23), 234702, DOI: 10.1063/1.4840675.

34 C. Arnal, M. U. Alzueta, A. Millera and R. Bilbao, Experimental and kinetic study of the interaction of a commercial soot with NO at high temperature, *Combust. Sci. Technol.*, 2012, **184**(7–8), 1191–1206, DOI: 10.1080/00102202.2012.664010.

35 A. Setiabudi, M. Makkee and J. A. Moulijn, The role of NO_2 and O_2 in the accelerated combustion of soot in diesel exhaust gases, *Appl. Catal. B Environ.*, 2004, **50**(3), 185–194, DOI: 10.1016/j.apcatb.2004.01.004.

36 C. Steuwe, *et al.*, Rapid and label-free optical detection of individual carbon air pollutant nanoparticulates in biomedical samples, *J. Biophotonics*, 2018, **11**(5), e201700233, DOI: 10.1002/jbio.201700233.

37 N. Li, M. Hao, R. F. Phalen, W. C. Hinds and A. E. Nel, Particulate air pollutants and asthma: a paradigm for the role of oxidative stress in PM-induced adverse health effects, *Clinical Immunology*, 2003, **109**(3), 250–265, DOI: 10.1016/j.clim.2003.08.006.

38 H. Bové, *et al.*, Combustion-derived particles inhibit *in vitro* human lung fibroblast-mediated matrix remodeling, *J. Nanobiotechnology*, 2018, **16**, 82, DOI: 10.1186/s12951-018-0410-x.

39 X. Chen, O. Nadiarynkh, S. Plotnikov and P. J. Campagnola, Second harmonic generation microscopy for quantitative analysis of collagen fibrillar structure, *Nat. Protoc.*, 2012, **7**, 654–669, DOI: 10.1038/nprot.2012.009.

40 N. J. Durr, C. T. Weissfennig, B. A. Holfeld and A. Ben-Yakar, Maximum imaging depth of two-photon autofluorescence microscopy in epithelial tissues, *J. Biomed. Opt.*, 2011, **16**(2), 026008, DOI: 10.1117/1.3548646.

41 T. Hoffmann, K. Kimura, T. Kimura and M. Fiebig, Second harmonic generation spectroscopy and domain imaging of the high-temperature multiferroic CuO, *J. Phys. Soc. Japan*, 2012, **81**, 124714, DOI: 10.1143/JPSJ.81.124714.

42 G. S. Boltaev, R. A. Ganeev, P. S. Krishnendu, K. Zhang and C. Guo, Nonlinear optical characterization of copper oxide nanoellipsoids, *Sci. Rep.*, 2019, **9**, 11414, DOI: 10.1038/s41598-019-47941-8.

43 M. E. Sadat, *et al.*, Photoluminescence and photothermal effect of Fe_3O_4 nanoparticles for medical imaging and therapy, *Appl. Phys. Lett.*, 2014, **105**(9), 091903, DOI: 10.1063/1.4895133.

44 D. Shi, M. E. Sadat, A. W. Dunn and D. B. Mast, Photofluorescent and magnetic properties of iron oxide nanoparticles for biomedical applications, *Nanoscale*, 2015, **7**, 8209–8232, DOI: 10.1039/c5nr01538c.

45 N. Zohora, *et al.*, Fluorescence brightness and photostability of individual copper (I) oxide nanocubes, *Sci. Rep.*, 2017, **7**, 16905, DOI: 10.1038/s41598-017-17295-0.

46 S. Dagher, Y. Haik, A. I. Ayesh and N. Tit, Synthesis and optical properties of colloidal CuO nanoparticles, *J. Lumin.*, 2014, **151**, 149–154, DOI: 10.1016/j.jlumin.2014.02.015.

47 M. Beversluis, A. Bouhelier and L. Novotny, Continuum generation from single gold nanostructures through near-field mediated intraband transitions, *Phys. Rev. B: Condens. Matter Mater. Phys.*, 2003, **68**, 115433, DOI: 10.1103/PhysRevB.68.115433.

48 T. Haug, P. Klemm, S. Bange and J. M. Lupton, Hot-Electron Intraband Luminescence from Single Hot Spots in Noble-Metal Nanoparticle Films, *Phys. Rev. Lett.*, 2015, **115**, 067403, DOI: 10.1103/PhysRevLett.115.067403.